Ice motion across incised fjord landscapes

Sjur Barndon[1, a], Robert Law[1, 2, 3, 4], Andreas Born[1, 2], Thomas Chudley[5], and Stefanie Brechtelsbauer[6]

[1]University of Bergen, Department of Earth Science, Norway
[2]Bjerknes Centre for Climate Research, Norway
[3]Laboratory of Hydraulics, Hydrology and Glaciology (VAW), ETH Zurich, Zurich, Switzerland
[4]Swiss Federal Institute for Forest, Snow and Landscape Research (WSL), bâtiment ALPOLE, Sion, Switzerland
[5]Durham University, Department of Geography, UK
[6]Stockholm University, Department of Meteorology, Sweden
[a]Now at University of Bergen, Department of Biological Sciences, Norway

Correspondence: Sjur Barndon (sjurbarndon@proton.me)

Abstract.

The thermodynamic behaviour of ice-sheet motion over rough landscapes is poorly understood, with most ice-sheet models prescribing a bed smoother than reality, which ~~will~~ does not fully capture topographic features. Subglacial fjords striking obliquely to the palaeo flow direction are an ~~extreme case~~end member of this misrepresentation, but are ubiquitous beneath the western margin of the palaeo Scandinavian Ice Sheet, and ~~likely~~ provide a useful proxy for areas of the present-day Greenland Ice Sheet. Here, we consider Veafjorden as a characteristic western Norwegian fjord where striations clearly evidence palaeo perpendicular ice flow, and perform 3D thermodynamically-coupled ice-motion simulations across a range of orientations. For perpendicular flow, ~~surface velocity above the fjord is reduced substantially while a thick layer of temperate ice occupies the fjord.~~ Moffatt eddies, or spiralling flows, occur within a thick layer of temperate ice in the fjord hollow with reverse-direction slip at the fjord base. ~~When compared to smoothed topography , perpendicular flow over *real* topography requires $\sim$~~Area-averaged driving stress in simulations with real topography and fjord-perpendicular flow is $\sim$41–89% greater than in simulations with smoothed topography for an equivalent surface velocity. In comparison, simulations with fjord-perpendicular flow show $\sim$28–45% greater area-averaged driving stress ~~, dependent on the overlying ice thickness, while a switch from~~ than simulations with fjord-parallel ~~to fjord-perpendicular flowfor real topography requires a $\sim$28–45% area-averaged driving-stress increase~~flow. The steep slopes of fjords and other similar features also provide a clear physically-based example for why bounded basal traction relationships (i.e. regularised-Coulomb) may not hold at the macro scale in rough settings. These results may explain surface velocity variations at many locations towards the margins of the Greenland Ice Sheet, and imply that the role of anisotropic roughness in resisting ice-sheet motion may be ~~significantly underappreciated. Last, we note that deep fjords provide a clear physically-based example for why bounded basal traction relationships (i.e. regularised-Coulomb) may not hold at the macro scale in rough settings.~~ under-appreciated.

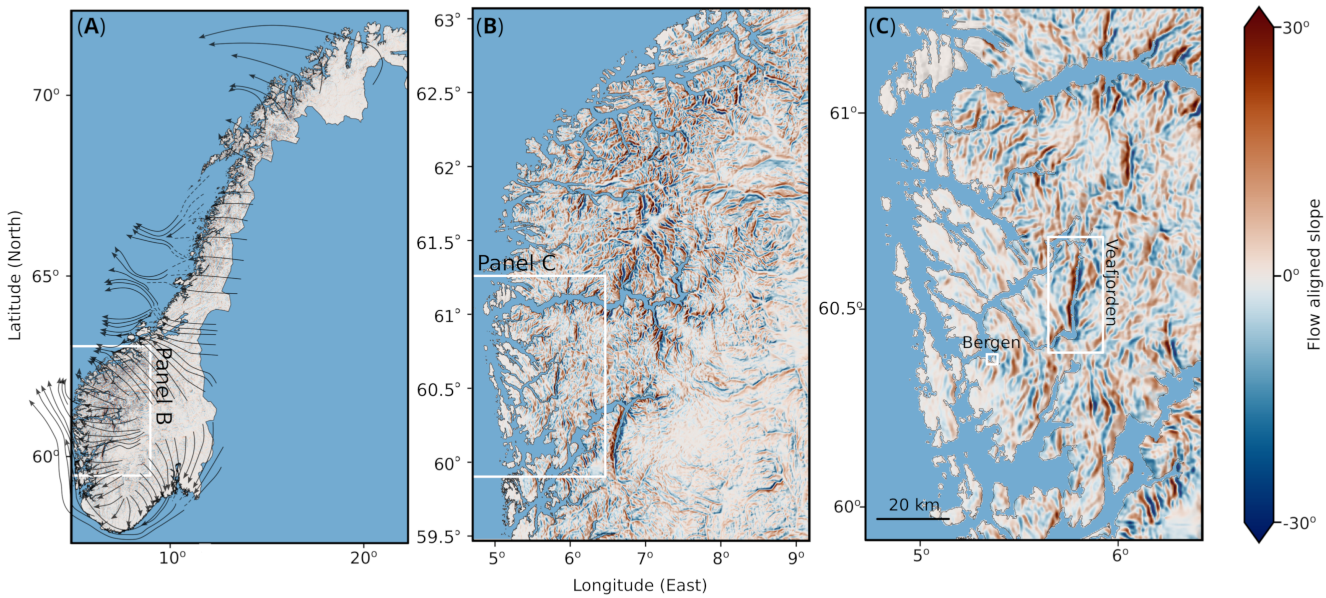

Figure 1. Slope calculated using the flow direction output of Jungdal-Olesen et al. (2024) for 32 kyr ago with Copernicus GLO-30 DEM data (Copernicus DEM, 2024). Positive values indicate an increase in elevation along the flow direction. Note that the maximum resolution of 60 m in panel C means that some small features (i.e. cliffs) may not be accurately resolved. Flow arrows in panel A adapted from Ottesen et al. (2005).

1 Introduction

Basal topography exerts a critical control on ice-sheet motion at all scales considered (Kyrke-Smith et al., 2018; Helanow et al., 2021; Castleman et al., 2022; Frank et al., 2022; Wernecke et al., 2022; Law et al., 2023), but ~~its~~ it's influence at the intermediate scale ~~— above the ∼~~– between the 0.5-25 m scale typically used to determine sliding parametrisations ~~yet below the ∼~~and the 400-4,000 m scale ~~of resolution or basal topography fidelity of most ice sheet models —~~ typical of ice-sheet model fidelity – is particularly poorly ~~constrained~~understood. Notably, the ice-motion influence of incised fjord landscapes remains almost entirely unexplored. This landscape characterises the terrestrial western margin of the palaeo Scandinavian Ice Sheet and provides a reasonable proxy for marginal areas of the Greenland Ice Sheet (GrIS) which share geological and topographic similarities (e.g. Gee et al., 2008; Christ et al., 2023; Paxman et al., 2024), as well as regions of the Antarctic Ice Sheet (AIS) such as the Aurora Subglacial Basin (Young et al., 2011). In ~~the fjords of~~ western Norway, glacial striations (Kleman et al., 1997; Mangerud et al., 2019) and ~~consideration of palaeo~~ paleoglacial flow directions (Jungdal-Olesen et al., 2024) ~~evidence widespread~~ show perpendicular ice flow over deep subglacial fjords, as well as in ~~obtuse~~ oblique and parallel orientations (Fig. 1)~~with unclear~~. The implications for ice motion in these flow scenarios remain unclear.

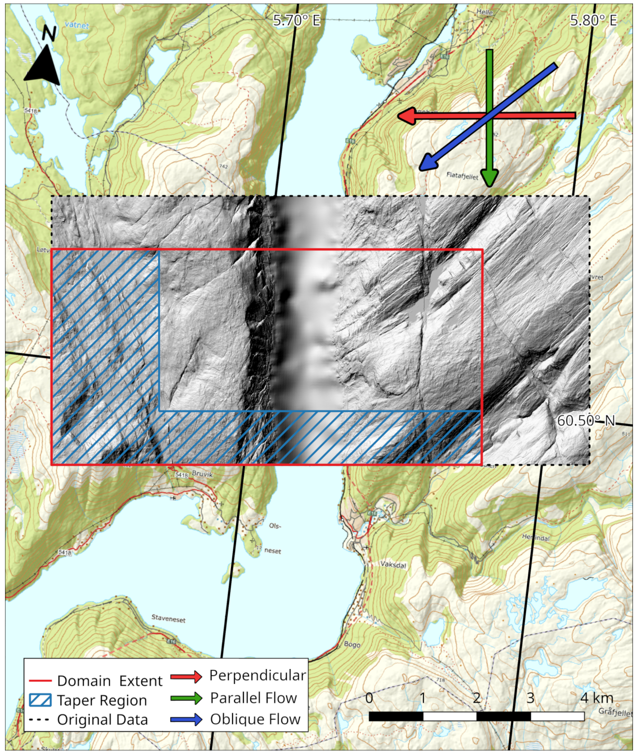

Figure 2. DEM of Veafjorden. The blue hatched area show the tapering region used in all simulations. The red, blue and green arrows displays the simulated flow directions. Perpendicular flow (red arrow) have been dated to 15 kyr BP and parallel flow (green arrow) at 11.5 kyr BP (Mangerud et al., 2019). Elevation data from the Norwegian Mapping Authority (Kartverket, 2024b, a).

~~Ice motion across an idealised subglacial valley has been modelled in 2D and 3D in a relatively straightforward manner (Gudmundsson, 1997; Meyer and Creyts, 2017), but not previously using actual topographic data and with the inclusion of temperate ice rheology, implementation of a rate-dependent resistance for slip at the ice-bed boundary, or 'fast' ($\geq$100 m a^{-1}) ice-surface velocity.~~ Here, we ~~incorporate these additional processes and consider fast ice motion for a section of the palaeo Scandinavian Ice Sheet. We~~ focus on Veafjorden close to the city of Bergen, Norway (Fig. 2) as a characteristic example with a relief of $\sim$ 1,300 m, and a narrow $\sim$2 km width. Striation markings on both sides of Veafjorden confirm near-perpendicular flow across the fjord around 15 kyr ago (Mangerud et al., 2019). The Norwegian fjords were likely incised into pre-existing river valleys and geological weaknesses through erosion as the Scandinavian Ice Sheet grew and shrank, but not at its fullest extent ~~(Harbor et al., 1988; Harbor, 1992; Briner et al., 2008; Bernard et al., 2021; Paxman, 2023; Reilly, 2023; Jungdal-Olesen et al., 2024), however the general pattern of fjord formation in western Norway has not been comprehensively investigated to our knowledge.~~ (Harbor et al., 1988; Harbor, 1992; Briner et al., 2008; Bernard et al., 2021; Paxman, 2023; Reilly, 2023; Jungdal-Olesen et al., 2024; Egh . In common with a comparable study from south-west South America, it may be that geological factors, rather than inherent glaciological instabilities (Kessler et al., 2008), exert a a first-order control on fjord orientation.

Ice motion perpendicular to idealised subglacial valleys has previously been modelled in 2D and 3D (Gudmundsson, 1997; Meyer and Cr , with Meyer and Creyts (2017) investigating the role of a critical angle in V-shaped valleys to predict the onset of Moffatt eddies (spiralling ice flow that form in topographic hollows). However, these studies did not include real topographic data, temperate ice rheology, or rate-dependent resistance for slip at the ice-bed boundary. Here, we incorporate these additional processes and consider fast ice motion for a section of the palaeo Scandinavian Ice Sheet. In order to assess the difference in controls on ice motion between this *real* topography, and the smoother bed products used to model the GrIS and AIS (BedMachine and BedMap), we ~~additionally~~ create a smoothed representation of Veafjorden (henceforth referred to as the smoothed topography). This substitute provides ~~an opportunity~~ the basis to examine the impact of the generally low fidelity elevation models presently in use.

~~Our simulationscan therefore~~ The simulation ensemble consists of 16 simulations, each with a unique ice flow scenario. The varying parameters are (1) target surface velocity, (2) flow direction – parallel, oblique and perpendicular to the fjord incision (See Fig. 2) – and (3) plateau ice thickness. We also perform 4 comparison simulations with the smoothed topography. The smoothed topography simulations have perpendicular flow direction while target surface velocity and plateau ice thickness are still varied. By simulating Veafjorden with both the smoothed topography and the *real* topography, we reveal the influence of realistic anisotropic basal conditions ~~.~~ and limited bed topography fidelity in ice-sheet models.

Over a single glacial cycle, the orientation of ice motion ~~will vary~~ varies (Jungdal-Olesen et al., 2024), while the landscape ~~will remain~~ remains effectively immutable. The simulations presented here, and consideration of how these extend to the broader palaeo Scandinavian Ice Sheet, indicate that over ~~rough~~ anisotropic topography complex basal motion patterns should be expected as the norm rather than the exception. Finally, while our simulations reveal ice thermodynamics over fjords in great detail, considerations of simple aspects of fjord geometry ~~and viscous ice deformation within them further~~ point towards the influence such landscapes should exert on intermediate, or macro, scale sliding relationships.

2 Methods

We model 3D ice motion over an 8 km by 4 km rectangular domain covering Veafjorden (Fig. 2). The Digital Elevation Model (DEM) was constructed at a resolution of 20 m with data from Kartverket (The Norwegian Mapping Authority), combining terrestrial data at 1 m (Kartverket, 2024b), with the fjord bathymetry interpolated from a 50 m resolution data set (Kartverket, 2024a). To conform to the ~~models~~ model's periodic boundary conditions the inflow and outflow boundaries must match. We achieved this using a tapering algorithm following Helanow et al. (2021), with one third of the down-flow length and width of the domain added as a tapering region that then matches the ~~topograhpy~~ topography at the inflow boundary (Fig. 2). We applied a Gaussian filter with a standard deviation of 1.5 to the DEM to smooth out artifacts and sharp edges which can present model stability issues (Law et al., 2023).

The domain was discretised in Elmer/Ice Version 9.0 (Gagliardini et al., 2013) with a triangular mesh with a representative element side length of 25 m and 20–30 vertical layers with resolution increasing towards the base (with a representative side length of 100 m and 15 vertical layers for the smoothed topography simulation with 500 m plateau ice thickness – ice thickness measured from the highest point in our domain). First, the free surface is allowed to vary and the inflow and outflow and two lateral boundaries are matched periodically for velocity, stress, and free-surface position. Second, the free surface and the inflow velocity fields are fixed and the enthalpy field is allowed to evolve without a periodic boundary condition requirement. Outflow/side boundaries are set at lithostatic pressure/zero flux depending on simulation orientation (Fig. A1).

The central equations and boundary conditions ~~are as follows, with additional model background in Law et al. (2023)~~ follow Law et al. (2023) with minor adjustments to geometric set up. Table A1 lists all parameter values. We solve the standard Stokes equations for ice flow

$$\nabla \cdot \boldsymbol{u} = 0 \qquad \text{(conservation of mass)} \tag{1}$$

$$\nabla \cdot \boldsymbol{\tau} - \nabla p = -\rho \boldsymbol{g} \qquad \text{(conservation of momentum)} \tag{2}$$

where $\boldsymbol{u}$ ($\mathrm{m\,a^{-1}}$) is the velocity vector, $\boldsymbol{\tau}$ (MPa) is the deviatoric stress tensor, p (MPa) is ice pressure, ρ (kg m^{-3}) is the ice density and $\boldsymbol{g}$ is the gravity vector described as

$$\boldsymbol{g} = [g\,\sin(\theta),\ 0,\ -g\,\cos(\theta)] \tag{3}$$

where $g = 9.81\ \mathrm{m\,s^{-2}}$ and θ is the domain slope. In simulations, the x-axis is oriented perpendicular to the fjord incision, and the y-axis along the fjord. The z-axes is normal to the horizontal plane, and does not match the $\boldsymbol{g}$ vector. Adjusting the orientation of $\boldsymbol{g}$ removes the requirement for vertical displacement of periodic inflow-outflow boundaries.

Stress is related to strain using the Nye-Glen isotropic flow law (Nye, 1953; Glen, 1955; Cuffey and Paterson, 2010):

$$\dot{\boldsymbol{\epsilon}} = A\tau_e^{n-1}\boldsymbol{\tau} \tag{4}$$

where $\dot{\boldsymbol{\epsilon}}$ (s^{-1}) is the strain rate tensor, $\tau_e^2 = \frac{1}{2}\mathrm{tr}(\boldsymbol{\tau}^2)$ (MPa) is the effective stress in the ice, n is the flow exponent set to ~~3, and A ($\mathrm{MPa^{-3}a^{-1}}$)is the creep parameter.~~ 3. The creep parameter, A ($MPa^{-3}a^{-1}$), varies depending on whether ice is above or below the pressure melting point T_m. For ice below T_m, A is set using the homologous temperature, T_h (K), ~~below the pressure melting point,~~ while ice above T_m, ~~or water fraction ,~~ is determined by the water fraction ω~~, when above the pressure melting point~~:

$$A = \begin{cases} A_1 \exp(\frac{Q_1}{RT_h}), & T_h \leq T_{\text{lim}} \\ A_2 \exp(\frac{Q_2}{RT_h}), & T_{\text{lim}} < T_h < T_m \\ (W_1 + W_2\omega \times 100)W_3, & T_h \geq T_m \text{ and } \omega < \omega_{\text{lim}} \\ A_{\max}, & \omega \geq \omega_{\text{lim}} \end{cases} \tag{5}$$

where $T_m(p) = T_{\text{tr}} - \gamma(p - p_{\text{tr}})$ and γ ($\mathrm{K\,MPa^{-1}}$) is the Clausius-Clapeyron constant, and T_{tr} and p_{tr} are the temperature and pressure triple points for water, respectively. A_1 and A_2 ($\mathrm{MPa\,a^{-1}}$) are rate factors, Q_1 and Q_2 ($\mathrm{J\,mol^{-1}}$) are activation energies for $T \leq T_{\text{lim}}$ and $T_{\text{lim}} < T < T_m$, respectively, where T_{lim} is the limit temperature. R ($\mathrm{J\,mol^{-1}}$) is the gas constant, W_1, W_2 and W_3 ($\mathrm{MPa\,a^{-1}}$) are water viscosity factors (constant for all simulations) with default values from Haseloff et al. (2019) adapted from Duval (1977). The liquid water fraction limit, ω_{lim} is set to 2.5% following experiments of Adams et al. (2021). If ω_{lim} is exceeded then A is limited to a maximum value A_{max}. Very recent studies propose $n = 1$, or different relationships for A for temperate ice (Schohn et al., 2025; Roldán-Blasco et al., 2025), but we leave exploration of these parameters for a future study. Values for these and subsequent parameters are provided in Table A1.

Within the Elmer/Ice EnthalpySolver (Gilbert et al., 2014), specific enthalpy, H (J kg^{-1}), is used as the state variable and is related to T and ω as

$$H(T,\omega) = \begin{cases} \frac{1}{2}C_a\left(T^2 - {T_{ref}}^2\right) & \\ \quad + C_b\left(T - T_{ref}\right), & H < H_m(p) \\ \omega L + H_m, & H \geq H_m(p) \end{cases} \tag{6}$$

where C_a (J kg^{-1} K^{-2}) and C_b (J kg^{-1} K^{-1}) are enthalpy heat capacity constants, L (J kg^{-1}), is the latent heat capacity of ice, $H_m(p) = \frac{1}{2}C_a\left(T_m(p)^2 - {T_{ref}}^2\right) + C_b\left(T_m(p) - T_{ref}\right)$ is the specific enthalpy at the pressure melting point, and T_{ref} is the reference temperature.

~~Change in the position of the free surface, s, is calculated as~~

$$\cancel{\frac{\delta s}{\delta t} + u_x\frac{\delta s}{\delta x} + u_y\frac{\delta s}{\delta y} = u_z}$$

~~in the Elmer/Ice FreeSurfaceSolver where $u_x, u_y,$ and u_z are components of $\boldsymbol{u}$.~~

At each time step, the enthalpy field is evolved until a steady-state is reached and is calculated as

$$\rho\left(\frac{\partial H}{\partial t} + \boldsymbol{u}\cdot\nabla H\right) = \nabla(\kappa\nabla H) + \text{tr}\left(\boldsymbol{\tau}\dot{\boldsymbol{\epsilon}}\right)$$

(conservation of energy) (7)

where $\text{tr}\left(\boldsymbol{\tau}\dot{\boldsymbol{\epsilon}}\right)$ is the strain heating term and κ (kg m^{-1} s^{-1}) is the enthalpy diffusivity defined as

$$\kappa = \begin{cases} \kappa_c, & H < H_m(p) \\ \kappa_t, & H \geq H_m(p) \end{cases} \tag{8}$$

where κ_c and κ_t are enthalpy diffusivities for cold and temperate ice respectively (Schoof and Hewitt, 2016), meaning that water movement within the temperate ice is assumed to be a diffusive process.

Change in the position of the free surface, s, is calculated as

$$\frac{\delta s}{\delta t} + u_x\frac{\delta s}{\delta x} + u_y\frac{\delta s}{\delta y} = u_z \tag{9}$$

in the Elmer/Ice FreeSurfaceSolver where $u_x, u_y,$ and u_z are components of $\boldsymbol{u}$.

The lower boundary velocity is set to zero normal to the surface (impenetrability condition at base):

$$\boldsymbol{u} \cdot \boldsymbol{n} = 0 \text{ where } z = 0 \tag{10}$$

where ~~$\boldsymbol{u}$ is the velocity vector and~~ $\boldsymbol{n}$ is the normal vector to the bedrock. Basal traction τ_b is calculated following Helanow et al. (2021) as:

$$\tau_b = C N_e \left(\frac{u_b^{-n+1}}{u_b + A_s C^n N_e^n} \right)^{\frac{1}{n}} u_b \tag{11}$$

where C (dimensionless) is a parameter dependant on basal morphology (Helanow et al., 2021). $N_e = p_i - p_w$ (MPa) is the effective pressure ~~at the bed~~ where p_i (MPa) is the ice overburden pressure and p_w (MPa) is the subglacial water pressure, with N set at 24% of p_i following Law et al. (2023). u_b ($\mathrm{m\,a^{-1}}$) is the basal velocity tangential to the ice-bed interface. The flow exponent n is the same as for the strain rate ~~equal to~~ and set as 3. A_s ($\mathrm{m\,a^{-1}\,MPa^{-3}}$) is the average sliding coefficient based on six values from Helanow et al. (2021).

2.1 Simulation ensemble

We simulate variations in flow direction, target surface velocity, and the thickness of ice over the plateau (measured from the highest point within the domain), as well as a smoothed control run with ice motion perpendicular to the fjord. We selected two ice thicknesses, 500 m and 1,000 m, both within the modelled ice thickness of previous studies (Svendsen and Mangerud, 1987; Mangerud et al., 2019) and which provide a reasonable range for exploring the role of ice thickness on flow patterns before fjord geometry begins to influence flow direction (Reilly, 2023). Two target surface velocities were selected, 450 $\mathrm{m\,a^{-1}}$ and 850 $\mathrm{m\,a^{-1}}$, based on the surface velocity at bore-hole locations with matching ice thickness in Greenland (Løkkegaard et al., 2023). Three flow directions are simulated, perpendicular (90°), oblique (45°) and parallel (0°). An overview of all simulations can be found in Table 1 and Fig. 3. The smoothed topography was created by applying a Gaussian filter with a standard deviation of 50 grid cells to the original DEM.

To reach a target surface velocity, a low fidelity (resolution of 100 m with 10 extruded mesh levels) simulation was used with an ad-hoc approach to tests using increments of 0.05° for θ. The value that produced the closest-to-target average surface velocity (values displayed in Table 1) was then used in subsequent full-resolution simulations. We convert the resulting slope to driving stress for comparison. Driving stress, τ_d, is calculated from domain-averaged ice thickness, ~~H~~ H_{av}, and the slope used to adjust the gravity vector orientation, θ, as

$$\tau_d = \rho g H \cancel{sin}_{\text{av}} \sin(\theta). \tag{12}$$

~~Note that the H~~ The domain-averaged ice thickness, including the fjord hollow, used in τ_d is ~~the average ice thickness of the domain giving~~ 1398.6 m and ~~898.6 m for~~ 989.6 m for plateau ice thickness values of 1,000 m and 500 m~~above the plateau~~, respectively. The smoothed topography DEM yields ~~the~~ averages of 1222.6 m and 722.6 m for plateau ice thickness 1,000 m and 500 m respectively.

3 Results

Our results demonstrate the strong control that subglacial fjords ~~,~~ and their orientation ~~with respect to ice motion direction,~~ exert on ice-sheet motion (Fig. 3). For flow-perpendicular simulations, Moffatt eddies and basal flow reversal occurs for both 500 m and 1,000 m ice thickness above plateau, but only with real (i.e. not smoothed) topography. Deep perpendicularly-oriented valleys beneath an ice sheet also significantly impede overlying ice motion — comparing one smoothed simulation (8Sm10, see Table 1) to its real topography counterpart (8Pe10) yields an increase in slope of 25.8%, equivalent to a change in area-averaged driving stress from 295.2 – 424.8 kPa (44%). Alternative fjord orientations also significantly influence both motion patterns and temperate ice distribution patterns. Here, we cover the following aspects: (3.1) perpendicular flow and the associated formation of Moffat eddies, (3.2) parallel flow, and (3.3) separation of flow in oblique-orientation simulations. Last, (3.4) we compare smoothed-topography control simulations to their real counterparts.

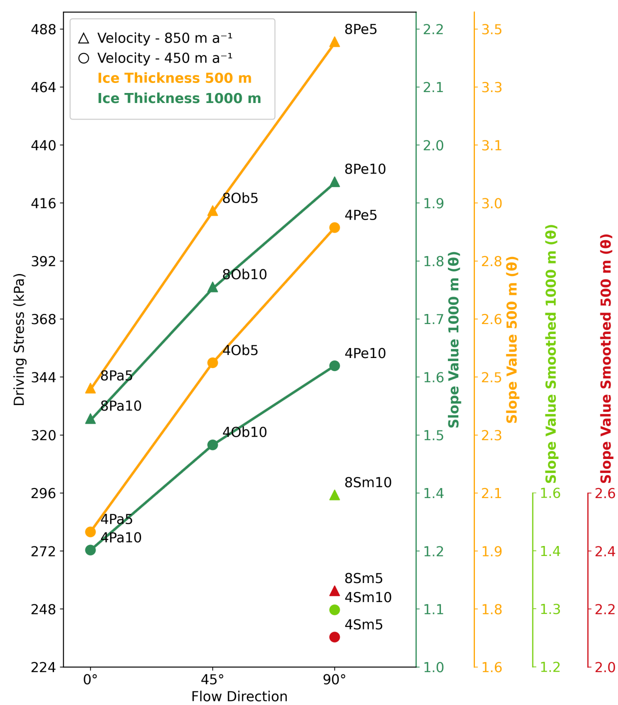

Figure 3. Resulting driving stress values for each selected flow direction, ice thickness and velocity target. Simulations with velocity target of 450 $\mathrm{m\,a^{-1}}$ are marked with circles, while 850 $\mathrm{m\,a^{-1}}$ are triangles. Simulations in green have a plateau ice thickness of 1,000 m while orange indicates a 500 m thickness. Average ice thickness was used in the driving stress calculation. Smoothed topography simulations have separate ice thickness values (See 2.1). The label for each marker are individual run IDs corresponding to Table 1.

Table 1. An overview of simulated scenarios and results. Flow direction is relative to the orientation of Veafjorden. Ice thicknesses are defined from the highest point of the domain. Simulation IDs reflect the variables used, ordered by velocity target, flow direction, and ice thickness. ~~For~~ An example ID is 8Pe10, describing the ~~base~~ reference simulation of Veafjorden with target surface velocity of 850 perpendicular flow, and plateau ice thickness of 1,000 m~~is 8Pe10~~. The corresponding simulation with 500 m plateau ice thickness ~~is~~ has the ID 8Pe5.

Target Surface Velocity ($\mathrm{m\,a^{-1}}$)	ID	Flow Direction	Plateau Ice Thickness (m)	Slope θ (°)	Driving Stress (kPa)	~~ID~~ Surface Velocity Mean ($\mathrm{m\,a^{-1}}$)	Target Velocity Deviation ($\mathrm{m\,a^{-1}}$)
450 m/a	4Pe10	Perpendicular	1,000	1.60	348.61	~~4Pe10~~ 479.8	29.8
	4Pe5		500	2.90	405.8	~~4Pe5~~ 531.4	81.4
	4Pa10	Parallel	1,000	1.25	272.4	~~4Pa10~~ 482.4	32.4
	4Pa5		500	2.00	279.9	~~4Pa5~~ 418.1	-31.9
	4Ob10	Oblique	1,000	1.45	315.9	~~4Ob10~~ 464.1	14.1
	4Ob5		500	2.50	349.9	~~4Ob5~~ 463.2	13.2
	4Sm10	Perpendicular	1,000	1.30	247.6	~~4Sm10~~ 468.3	18.3
	4Sm5	(Smoothed Control)	500	2.10	236.4	~~4Sm5~~ 478.7	28.9
850 m/a	8Pe10	Perpendicular	1,000	1.95	424.8	~~8Pe10~~ 844.3	-5.7
	8Pe5		500	3.45	482.7	~~8Pe5~~ 871.4	21.4
	8Pa10	Parallel	1,000	1.50	326.8	~~8Pa10~~ 860.3	10.3
	8Pa5		500	2.425	339.4	~~8Pa5~~ 872.0	22.0
	8Ob10	Oblique	1,000	1.75	381.3	~~8Ob10~~ 829.2	-20.8
	8Ob5		500	2.95	412.8	~~8Ob5~~ 837.4	-12.6
	8Sm10	Perpendicular	1,000	1.55	295.2	~~8Sm10~~ 868.4	18.4
	8Sm5	(Smoothed Control)	500	2.27	255.5	~~8Sm5~~ 815.3	-34.7

3.1 Perpendicular flow direction

Across all target velocities and plateau ice thickness combinations for perpendicular flow over real topography Moffatt eddies (Moffatt, 1964a, b) form at the base of the fjord, accompanied by spiralising lateral ice motion along the lowermost fjord depression. Ice velocity is also greatly affected by the topography. ~~For~~ In simulations with target surface velocity of 850 $\mathrm{m\,a^{-1}}$ (8Pe10), the surface velocity directly above the fjord ~~velocity is reduced by~~ is ~120 $\mathrm{m\,a^{-1}}$ lower than the maximum (Fig.7d)~~, while absolute~~. Absolute velocity within the fjord ~~the plateau elevation drops below~~ (below the elevation of the plateau) drops to less than 500 $\mathrm{m\,a^{-1}}$ (Fig. 4c). This velocity difference creates a distinct shear margin that spans the fjord from crest to crest across the width of the entire domain (Fig. 4). The eddies that form under this sheer margin are up to 570 m in diameter. In the case of simulation 8Pe10 with target velocity of 850 $\mathrm{m\,a^{-1}}$ and ice thickness of 1,000 m a secondary set of eddies is also simulated (Fig. 5b).

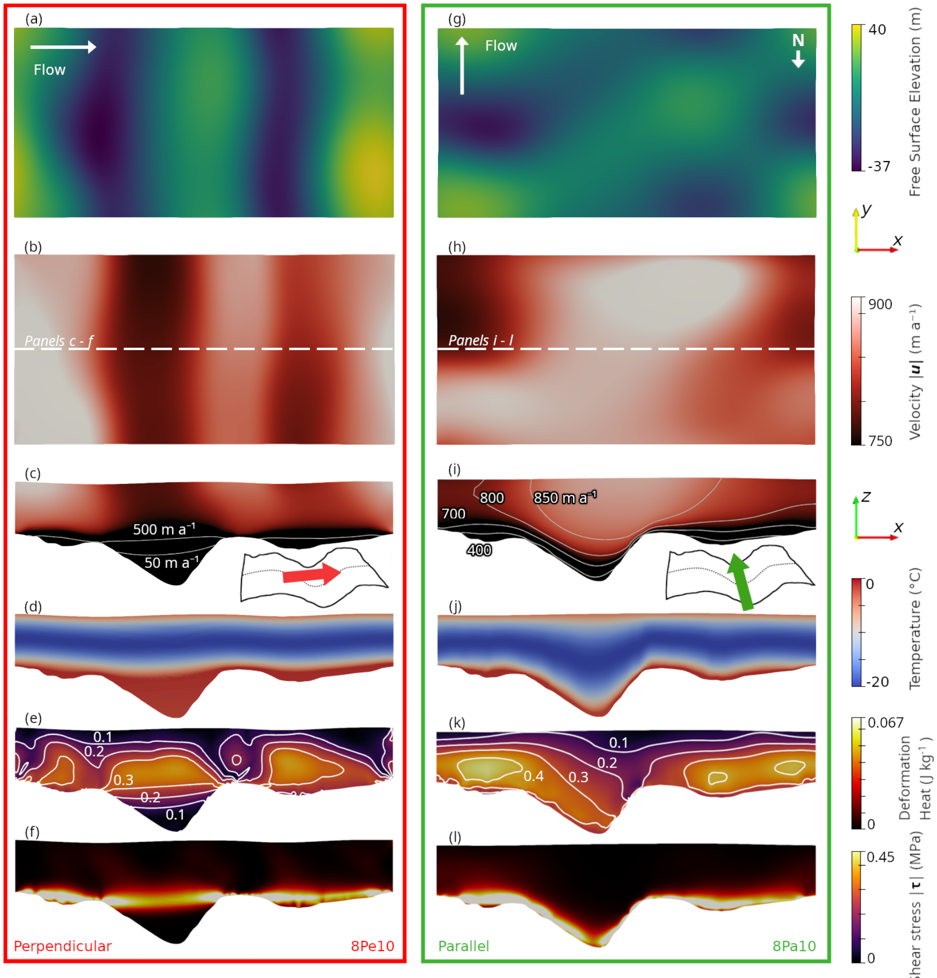

Figure 4. Free surface elevation and velocity of perpendicular 8Pe10 **(a–f)** and parallel 8Pa10 **(g–l)** simulations. Panel **(a, g)** show the free surface elevation, **(b, h)** show the corresponding surface velocity (m a^{-1}). Panel **(c, g)** is the velocity field of the cross section from the centre of the domain. Panel **(d, h)** show temperature (C°) at the same cross section. Panel **(e, k)** show deformation heat (J kg^{-1}) and panel **(f, l)** is the shear stress (MPa).

Flow from the tributary valley on the upslope plateau, feeds ice flow into the Moffatt eddies. Upon entering the fjord from the tributary, the Moffatt eddy splits laterally, resulting in two independent eddies transporting ice in opposite directions along the fjord. In the free surface runs where periodic lateral boundaries are present (and temperate ice is not) ice is exchanged laterally through the boundary in both positive and negative y orientations, as well as returning back to the main overriding flow. When no-flux boundaries replace lateral periodic boundaries in the thermomechanically coupled runs more ice is directed back into the overriding flow towards the domain edges. The maximum y-oriented velocity within the fjord is $\sim$27 m a^{-1} (8Pe10).

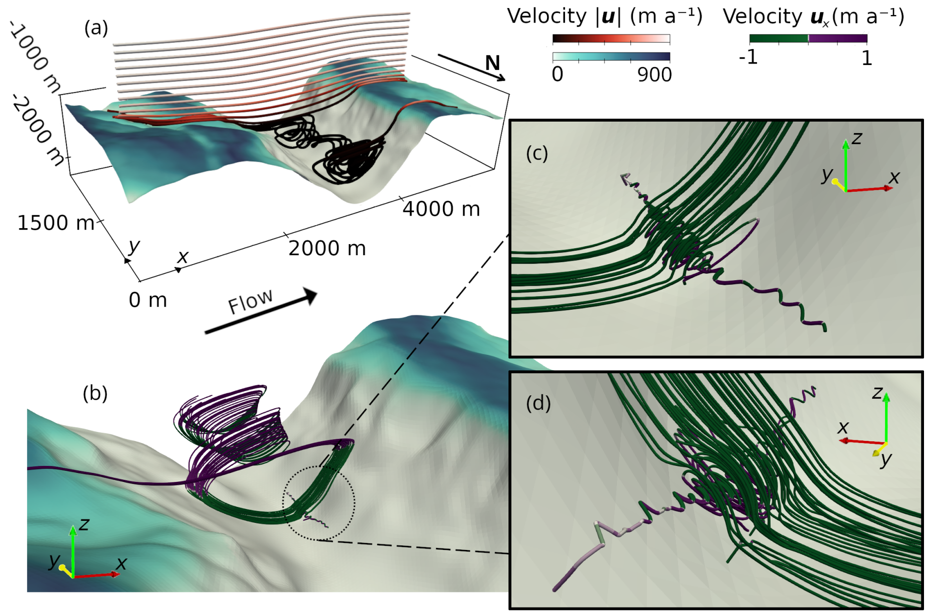

Figure 5. Streamline velocity for perpendicular, 1,000 m plateau ice thickness run 8Pe10. Streamlines show that ice from the plateau enters an eddy in the valley, moves laterally, and reappears far to the north on the other side **(a)**. Streamlines of **(a)** coloured by velocity magnitude. ~~Secondary~~ A secondary Moffatt eddy ~~forms~~ is formed in a small depression in the valley side ~~(b)~~(**b**–**d**). Panel (**c**) show the larger eddy streamlines flowing from right to left, while the smaller eddy spins counter clockwise in the topographic depression. Panel (**d**) shows the same secondary Moffatt eddy as in (**c**) from the opposite side. Streamlines coloured for x direction velocity **(b–d)**, constrained from -1 to 1 $\mathrm{m\,a^{-1}}$ showing reversal of flow. Target surface velocity 850 $\mathrm{m\,a^{-1}}$.

Just below the margin between the Moffatt eddies in the fjord, and the overflowing ice above, there is a reduction in liquid water content. Partial refreezing of meltwater occurs as the eddies rise on the up-slope fjord side (Fig. 6a.ii). From a Lagrangian viewpoint, the rise increases the pressure melting point and lowers the specific enthalpy at the pressure melting point ($H_m(p)$) meaning the melt fraction decreases so that the overall specific enthalpy does not change. This temperate ice water content margin is present along the entire valley, following the meeting point between eddy movement and overlaying ice (Fig. 6a.i). High stresses and deformation heating between the fjord crests (Fig. 4e,f) results in the formation of a deep temperate layer found in perpendicular simulations (Fig. 6a).

3.2 Parallel flow direction

We use the domain slope and hence domain-averaged driving stress as the main lever to adjust the area-averaged surface velocity. Considering a change in flow direction from parallel to perpendicular over the real topography with an ice thickness above the plateau of 1,000 m, the slope must be altered by 0.45°, corresponding to an increase in averaged driving stress from 326.8 to 424.8 kPa (30%) (8Pa10 and 8Pe10 respectively). This substantial difference in driving stress between parallel and

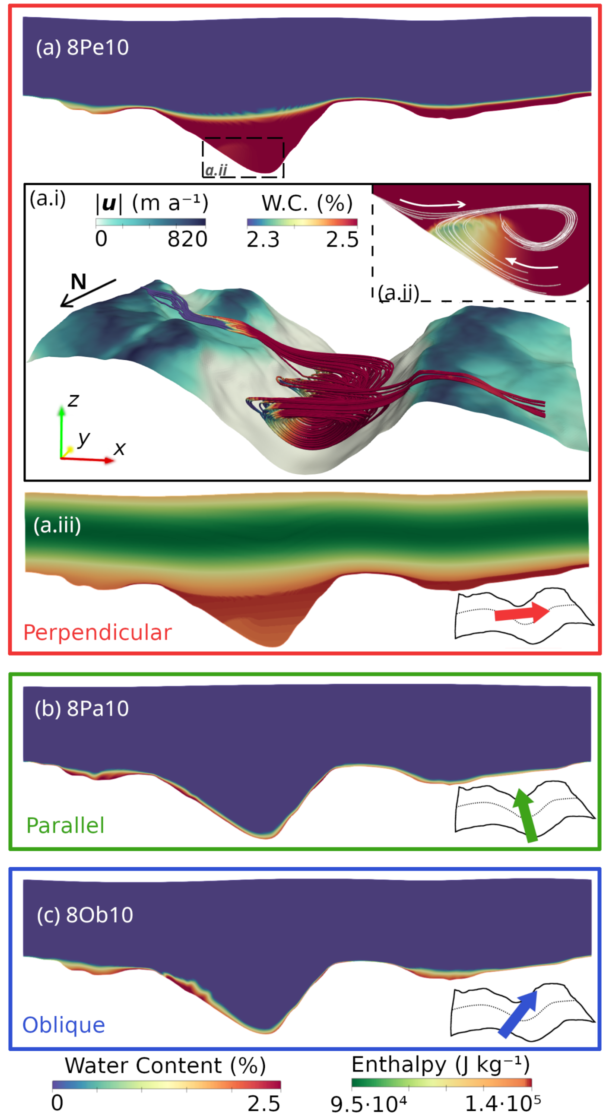

Figure 6. Temperate ice water content comparison of perpendicular **(a)**, parallel **(b)**, and oblique **(c)** flow direction. Cross sections taken from the centre of the domain. Panel **(a.iii)** show the enthalpy field of the same cross-section as **(a)**. A change in enthalpy can be spotted along the same margin where the temperate ice water content is reduced in the fjord.

perpendicular flow indicates the anisotropic nature of a landscapes resistance to flow dependent on its orientation (Fig. 4). The change in slope required to match surface velocity for parallel and perpendicular topography is similar to the difference between actual bed topography and the smoothed topography (0.40° for simulations 8Pe10, 8Sm10) when both are in the perpendicular orientation (Table 2). The influence of a parallel oriented-fjord on ~~surface elevation~~ ice surface position and velocity is fairly small, with a much more uniform decrease in velocity with depth when compared to the flow-perpendicular

Table 2. Mean slope and driving stress changes for varying simulation comparisons. Taking the average of the differences from all simulation flow directions, ice thicknesses and velocity targets. Smoothed control simulations are excluded from the velocity target comparison and the flow direction comparison.

Comparison			Mean Slope Difference(°)	Mean Driving Stress Difference (kPa)	Mean Driving Stress Change (%)
Parallel flow (IDs: *Pa**)	→	Perpendicular flow (IDs: *Pe**)	0.68	110.9	36.3
Perpendicular (Smoothed) (IDs:*Sm**)	→	Perpendicular flow (IDs:*Pe**)	0.67	156.8	61.3
450 $\mathrm{m\,a^{-1}}$ (IDs: 4****)	→	850 $\mathrm{m\,a^{-1}}$ (IDs: 8****)	0.39	65.9	18.5

simulations. The temperate ice layer thickness for parallel runs is uniformly much lower than for perpendicular runs, with no large volume of temperate ice occupying the fjord hollow (Fig. 6b).

3.3 Oblique flow direction

In the simulations with oblique flow the flow direction is vertically stratified. At the base of the fjord, the flow aligns with the fjord orientation, while surface flow aligns with the surface slope (Fig. A3). However, surface flow does not directly follow the domain slope (Eq. 3), but deviates from it due to the topographic steering at depth. The simulation with 1,000 m plateau ice thickness and target velocity of 450 $\mathrm{m\,a^{-1}}$ (4Ob10) has a surface flow direction change of 17.1° while the corresponding simulation of 500 m plateau ice thickness (4Ob5) has a surface change of 29.2°. This illustrates how a retreating ice sheet settles into the terrain following flow that results in fjord formation. As with parallel simulations, the thickness of the temperate ice layer is consistently much lower than for perpendicular simulations (Fig. 6c).

3.4 Smoothed control simulation

The perpendicular simulation with 1,000 m plateau ice thickness and 850 $\mathrm{m\,a^{-1}}$ target surface velocity (8Pe10) has an area-averaged driving stress of 424.8 kPa when real topography is used. In comparison, the smoothed topography simulation (8Sm10) with equivalent parameters has an area-averaged driving stress of only 295.2 kPa. In this case using a smooth or low fidelity subglacial topography underestimates the driving stress ~~required for~~ with equivalent average surface velocity by 43.9%. This effect increases as plateau ice thickness decreases. Comparing the corresponding simulations at 500 $\mathrm{m\,a^{-1}}$ (8Pe5 and 8Sm5) gives a difference of 227.2 kPa or 88.9%. On average for all perpendicular simulations, this discrepancy is larger than comparing perpendicular flow to parallel flow at Veafjorden (Table 2).

After decreasing the slope by 0.40°, the smoothed topography simulation (8Sm10) has a similar surface flow field to the real topography simulation (8Pe10) (Fig. 7d,h). When comparing local surface velocity over the fjord, both slow down by roughly the same amount. The smoothed control is reduced to 778.1 $\mathrm{m\,a^{-1}}$ while the real topography simulation is reduced to 782.3

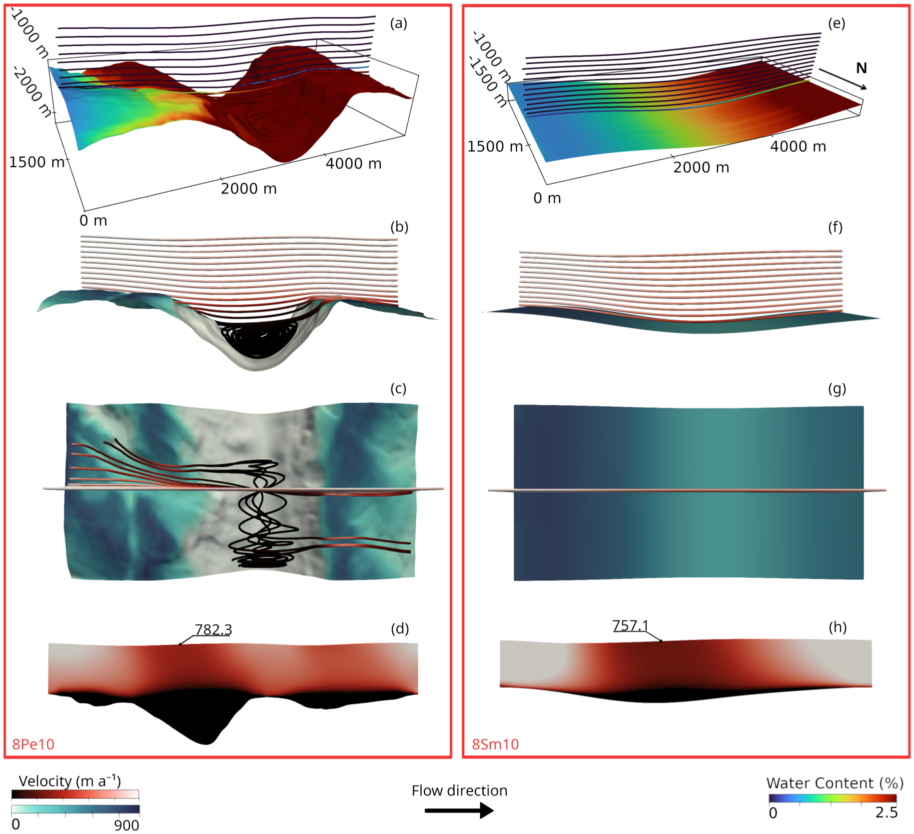

Figure 7. A comparison of Veafjorden perpendicular, 1,000 m plateau ice thickness, 850 m a^{-1} simulation to perpendicular smoothed control. Perpendicular Veafjorden 8Pe10 **(a–d)**. Perpendicular (Smoothed Control) 8Sm10 **(e–h)**. Note that panel (**d**) and (**h**) includes tapering region.

m a^{-1}. Both reach roughly 920 m a^{-1} at maximum. Nonetheless, the enthalpy fields, and hence rheological characteristics, between the two settings differ substantially (Fig. 7) with the water content in the control not approaching that of the real topography simulation. Furthermore, there is no indication of flow reversal or Moffatt eddies.

4 Discussion

Our results show that realistic fjord geometries — which are ~~(i)~~ common across the ~~western margin~~ margins of the palaeo-Scandinavian ice sheet ~~, (ii) likely present beneath the margins of the~~ and also likely across the present day GrIS, ~~and (iii) largely excluded from~~ yet which are largely excluded form large-scale ice-sheet models — significantly complicate patterns of ice motion and temperate ice. In contrast to smoothed topography, real topography can result in much higher driving stresses ~~required to achieve~~ in the same surface velocity setting, with clear evidence for a strong anisotropic response of ice motion to the alignment of the underlying landscape. ~~Features as dramatic as~~ Moffat eddies (Gudmundsson, 1997; Meyer and Creyts,

2017) ~~may at first appear to be~~ might seem like dramatic and isolated features with limited influence on overall ice-sheet motion~~:~~. However, our results and analysis of flow-aligned slope angles in western Norway (Fig. 1) suggest that ~~they are likely a ubiquitous feature of~~ these features are likely widespread in ice motion over incised fjord landscapes.

The complex flow patterns of Moffatt eddies are also dependant on topographic fidelity. The patterns of flow shown in our perpendicular simulations using real topography (Fig. 5a,b), including eddies and lateral transport along the fjord hollow, closely resemble the 3D simulations of Meyer and Creyts (2017) (their Fig.9). The idealised topography in these simulations invite ascribing a critical angle for Moffatt eddy formation. However, this is complicated somewhat by our use of real topography which does not fit as neatly as the triangular geometry found in (Meyer and Creyts, 2017). Nonetheless, an opening angle perpendicular to the fjord of $\sim 100°$ falls within the critical opening angle $\alpha_c = 134°$ for the rheological exponent $n = 3$ in (Meyer and Creyts, 2017), while the opening angle $\sim$170° for the smoothed simulation is above this α_c value. The opening angle along the prescribed 45° flow in the oblique simulations are $\sim 118°$ predicting Moffatt eddies to form. No eddies are seen in simulations with these settings. However, this may be explained by the shift in flow direction exerted by the topography (See Fig. A3d-f) further widening the opening angle. This indicates that a critical value may also have efficacy in predicting Moffat eddy occurrence in real settings but that low fidelity bed topography products where depressions such as fjords are not resolved are unlikely to be effective indicators of possible Moffat eddy locations.

Deep fjords furthermore present an obstacle to suggestions that basal traction should be treated as bounded across all glacier and ice-sheet settings (e.g. Schoof, 2005; Minchew and Joughin, 2020; Zoet and Iverson, 2020; Helanow et al., 2021). In bounded basal traction relationships (if effective pressure, N, is constant) the traction provided by the bed approaches a maximum value that it does not exceed (such as the regularised-Coulomb relationship used ~~as the base for~~ for individual elements in this model, Eq. 11)~~, while in~~. Whereas, an unbounded basal traction ~~relationships basal traction will continue increasing as basal velocity increases (such as Weertman sliding, Weertman (1957)~~relationship shows a continuous increase in basal shear stress with basal velocity (i.e. Weertman, 1957). For hard beds, the suggestion of bounded basal traction follows from Iken's bound (Iken, 1981; Schoof, 2005), usually defined as

$$\frac{\tau_b}{N} \leq \tan(\beta) \tag{13}$$

where τ_b is the basal traction ~~, $N = p_i - p_w$ is the effective pressure at the base where p_i and p_w are ice and water pressures respectively, and~~ and β is the maximum up-slope angle in the mean flow direction. However, Eq. 13 ceases to become an effective bound in the situation of very steep surfaces ~~, and furthermore omits traction provided at~~ (Gagliardini et al., 2007), and also omits any traction tangential to the ice-bed interface itself. In the case of ice flow ~~oriented perpendicular to~~ pressing perpendicularly against the near-vertical cliffs present on Veafjorden's western side (Fig. 8), there is no theoretical bound to the resistive traction that could be provided by the cliffs to oppose ice motion. If ~~the ice is effectively ‘locked in’ to the landscape as a result of rough topography, with very low, or even reversed basal slip (Fig. 5), then resistance to ice motion comes from the deformation of the ice itself which has a non-linear viscous rheology (Nye, 1953; Glen, 1955), or potentially even linear for temperate ice (Schohn et al., 2025; Adams et al., 2021). Taking a vertical line through the centre-point of the fjord in isolation, where velocity at the fjord base is ∼0.5-1 m~~ a ~~$^{-1}$ in the opposite direction to the surface orientation, resistance to driving stress,~~

~~τ_s, is then provided by viscous deformation within and below the shear band spanning the fjord hollow and can be expressed as~~

$$\tau_s = A \int_{z_b}^{z_s} (2\dot{\epsilon}_e)^{\frac{1}{n}} \, dz$$

~~where A and n refer to values in the Nye-Glen isotropic flow law (Eq. 4), $\dot{\epsilon}_e^2 = \frac{1}{2}\mathrm{tr}(\dot{\boldsymbol{\epsilon}}^2)$, and z_b and z_s refer to the positions of the fjord base and top of the shear band, respectively. If a~~ large-scale ~~ice sheet model~~ ice-sheet model then takes a smoothed basal surface rather than the actually existing rough topography, or if the discretisation of the model domain simply does not allow for features such as fjords to be accurately resolved (Fig. 8), then the shear-band features ~~such as those we simulate here for perpendicular flow will be implicitly subsumed into the basal sliding relationship – even if it is not expressly formulated or suitable for handling such deformation features. In the case of a deep fjord, it is simple to see how its entire span could be captured within a single ∼2 km numerical~~ and large slope values included in our simulations will create a situation, at least locally, where sliding is not well-described by a bounded sliding relationship limited by Iken's bound with a low value of β. Depending on the exact parameter choice, this could lead to a model grid cell ~~. If these features are inadvertently incorporated within sliding parameterisations we should expect at least a component of resistance to ice motion to follow an unbounded power-law (Eq. **??**), rather than ice-sheet sliding being bounded in all settings (Minchew and Joughin, 2020). Veafjorden is a dramatic example, but slopes, cliffs, and fjords which exceeding 30° in the palaeo flow direction are common across western Norway (Fig. 1), providing many more possible settings where resistance to ice motion is controlled by viscous ice deformation prompted by rough topography that would not otherwise be captured in~~ with a defined bounded sliding relationship being unable to provide a physically realistic amount of basal traction for that grid cell.

Classically, cavities may be anticipated to drown out high bed slopes in many instances thereby facilitating bounded basal traction (Schoof, 2005) – including in the inverted ellipsoid geometry of Gagliardini et al. (2007) which bears similarities to the across-fjord profile in our simulations. However, while these studies represent non-dimensionalised problems, their focus is not emphatically on large-scale features such as fjords and it is unintuitive to suggest that a cavity could be sustained within Veafjorden as there are clear hydrological escape pathways to the north and south (Figs. 1, 2). Therefore, while determining the configuration of subglacial cavities in a setting such as Veafjorden remains an important outstanding question for subglacial hydrology, we suggest it is likely that features such as Veafjorden provide major upslope resistance that is (i) not overcome by cavitation and (ii) not captured by the basal boundary position ~~used in large-scale ice sheet models.~~ of ice-sheet models.

Thus, the influence of Veafjorden and similar features on basal traction at the scale of discretised ice-sheet model grid cells (Fig. 8) may be closer to sliding studies where cavities are not permitted (such as Lliboutry, 1968, 1987; Fowler, 1981; Gudmundsson, 1997 and traction is unbounded, than to scenarios where cavities are permitted to overrun steep obstacles. Furthermore, features such as those modelled in this paper, even if sporadically placed, may still exert an important influence on regional ice-sheet motion through lateral and longitudinal stresses. ~~Further work is required to fully isolate these interactions and their scale dependence, but such~~ As slopes, cliffs, and fjords exceeding 30° in the palaeo flow direction are common across western Norway (Fig.

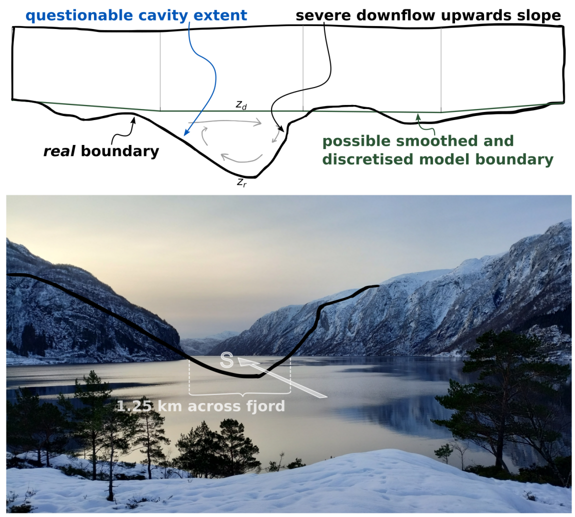

Figure 8. View of vertical cliffs on Veafjorden's western side. z_r and z_d are the real topography, and a possible discretised representation, respectively. The schematic profile is also traced onto the photo in black. Photo from Sergii Gryshyn taken from Fjordsyn Vaksdal Dagsturhytta.

1) and at least partially representative of the basal topography of the GrIS, we suggest that interactions with these features may go some distance ~~to~~ towards providing a physically based background to the persistent utility of unbounded power-law sliding relationships across the GrIS (Maier et al., 2021), which often invoke Weertman sliding (Weertman, 1957), even if the underlying assumptions are not entirely realistic (Weertman, 1979).

~~View of vertical cliffs on Veafjorden's western side from the E16 road at 60.508903 N, 5.725418 E. Image: ® Google, captured from Google Street View.~~

~~A possible barrier to this viewpoint is cavitation. In the two-dimensional settings of Schoof (2005) and Gagliardini et al. (2007) cavities gradually overwhelm geometric depressions as u_b increases, lowering τ_b. These two studies non-dimensionalise the domain such that the sinusoidal beds they use may be taken as an approximation of small-scale roughness or fjord geometry. However, Veafjorden features clear hydrological escape pathways both north and south (Figs. 1, 2). Combined with a palaeo ice sheet surface that would induce regional hydrological gradients towards the ocean, a very large cavity within Veafjorden in line with the models of Schoof (2005) and Gagliardini et al. (2007) seems unlikely. And, even in the perhaps implausible situation where a cavity occupies a space as large as the present day ocean within Veafjorden (Fig. 8), cliffs facing perpendicular to oncoming ice would still be present at the ice-bed interface. Regardless, determining the configuration of subglacial cavities in a setting such as Veafjorden, rather than a region that is approximately flat at the macro scale , remains an important outstanding question for subglacial hydrology~~Given ice sheet responses to changing climate are typically greater for bounded sliding relationships (Tsai et al., 2015), further work to fully asses the role of these features on ice-sheet basal traction fields at scale is well warranted.

~~The landscape of western Norway does not represent a one-to-one mapping of the subglacial landscape of Earth's presently existing ice sheets, but there are many similarities, particularly for~~ Ice motion across fjords may also help to explain features revealed in the surface velocity and surface position of the GrIS. ~~Areas of high relief (>1,000 m a.s.l.) with deep fjords are easily observable at both the western and eastern~~ Deep fjords exist across the ice-free margins of the GrIS, with the continuation of these fjords inland beneath the ice evident until BedMachine mapping begins to loose its sharpness (Morlighem et al., 2017). Flow-aware hill-shading of the GrIS surface (MacGregor et al., 2024) and analysis of radio-echo flight lines (Paxman et al., 2024) ~~also highlights locations across the GrIS~~ highlight multiple fast-flowing regions where ice flow is inferred to cross subglacial valleys perpendicularly ~~. In multiple fast-flowing regions close to the margins of the GrIS, inferred subglacial topography features from MacGregor et al. (2024)~~ and which appear to align with along-flow surface velocity variations in excess of 100 m a^{-1} ~~, reflecting~~ (Fig. A2). This reflects the surface velocity variations modelled in this study (Fig. ~~A2) . In Antarctica,~~ 4b,c) and indicates a similar topographic control could be at play. Similarly, such a mechanism could be important in East Antarctica where the Aurora Subglacial Basin and Gamburtsev Mountains ~~in particular exhibit~~ exhibit multiple subglacial valleys that cross cut the present-day prevailing flow direction ~~, which likely originated during the initial inception of the AIS (Young et al., 2011; Meyer and Creyts, 2017). Basal~~ (Young et al., 2011; Meyer and Creyts, 2017). Furthermore, basal traction inversions from both the GrIS and AIS ~~furthermore~~ evidence complex banded patterns~~(Sergienko et al., 2014) . In Sergienko et al. (2014) these are hypothesised~~ , hypothesised by Sergienko et al. (2014) to result from pattern-forming instabilities in subglacial water pressure. We suggest that they may in fact reflect varying resistance as a result of subglacial topography~~. Notably, this implies that the patterns are potentially much longer lasting than would be the case if they were solely a result of subglacial hydrology variations, and places an emphasis on the role of basal topography patterns on basal traction at the intermediate scale, rather than solely variations in basal material properties at the micro scale.~~ , indicating the potential influence of large scale topographic obstacles on basal traction fields derived from relatively smooth bed topography products.

Our results also ~~point to anisotropic resistance provided by subglacial landscapes, which has been previously explored in an idealised case (Hindmarsh, 2000). Given we look at topography from beneath a palaeo ice sheet, fjord orientations vary widely~~ illustrate the anisotropic resistance to ice-motion provided by real subglacial landscapes (Fig. ~~1~~3), and ~~our results indicate that ice-motion orientation variations significantly influence the resistance from topography~~ situations where the basal velocity vector may be non-parallel to its corresponding basal traction vector over a large area (Fig. ~~3) , we can conclude~~ A3) – previously explored in an idealised case by Hindmarsh (2000). This implies that basal traction patterns should be expected to vary over the lifecycle of an ice sheet, as drainage basins evolve and ice motion patterns shift during growth and decay. Bulk basal motion may furthermore be misaligned with the applied basal shear stress, which could result in complications for dynamic modelling where fine details are important. We leave direct quantification of the influence of landscape ~~anistropy~~ anisotropy on basal sliding relationship anisotropy for future work, but ~~also note~~ recognise that the impact of basal sliding anisotropy ~~will be~~ is likely small for most predictive timescales (100-1,000 yr) in the event that flow orientations do not shift substantially.

Last, geological evidence for the occurrence of the described flow patterns and Moffatt eddies is presently limited to the plateau striations surrounding Veafjorden (Mangerud et al., 2019). These striation markings indicate near-perpendicular flow across the fjord, but do not provide information about the motion within. Reverse direction striations within the valley are possible, but given subsequent ice-flow reorganisations (Mangerud et al., 2019; Reilly, 2023) it is likely that these lineations will have been removed by erosion or overwritten when ice flow switches to follow the fjord orientation.

5 Conclusions

We show that incised fjord landscapes induce significant complications into ice sheet motion~~, prompting a required increase in driving stress of up to~~ . Significantly greater ($\sim$41–89%~~when oriented perpendicular to flow~~) driving stresses are required to push ice perpendicularly over a fjord compared to smoothed topography~~. Realistic fjord topographies will also introduce anistropy into a landscapes basal traction response at a macro scale, and may furthermore invalidate the assumptions behind boundedtraction at these scales. It is evidently presently~~ , with a clear anisotropic response to fjord orientation apparent. Steep valley walls also present an obstacle not presently resolved in standard ice-sheet model bed products that may result in unbounded, rather than bounded, traction being appropriate and hence explain the efficacy of the power-law sliding relationships across large parts of the GrIS (Maier et al., 2021), which shares basal-topographic similarities with the paleo-Scandinavian Ice Sheet.

At present, it is infeasible and impractical to incorporate this behaviour into large-scale ~~ice sheet models directly due to computational limitations on resolution , with bed topography products furthermore lacking the fidelityto resolve such features~~ice-sheet models by increasing resolution and bed-product fidelity. Instead, ~~future work should focus on~~ parameterising the net influence of ~~this behaviour~~ the behaviour reported here — and that caused by other large-scale topographic obstacles — on basal traction relationships (and basal traction anisotropy) at the more relevant macro scale ~~, with particular reference to the viscous component of ice deformation that may unwittingly fall within the basal sliding relationship~~provides a reasonable pathway for future progress. Doing so may contribute to alleviating uncertainties in predictions of sea level rise (Aschwanden et al., 2021), and to reducing the share of uncertainty in basal traction inversions that pertains directly to sliding processes (Berends et al., 2023).

Code and data availability. Elmer/Ice solver input files, post-processing scripts, and ParaView visualisation files available at https://doi.org/10.5281/zenodo.15052902 (Barndon, 2025)

Appendix A: Calculating flow-aligned hill slope

To quantify the topographic gradient in the direction of surface flow, we computed the flow-aligned gradient using DEM data and flow velocity components. Partial derivatives of elevation in the x- and y-directions ($\frac{dz}{dx}$ and $\frac{dz}{dy}$, hereafter p and q, respectively) were computed from the DEM by fitting a third-order polynomial to a 5x5 window following Florinsky (2017). Flow direction was determined from velocity components v_x and v_y, with velocity magnitude $v_v = \sqrt{v_x^2 + v_y^2}$ used to compute unit vectors in the flow direction:

$$\hat{v} = \left(\frac{v_x}{v_v}, \frac{v_y}{v_v}\right) \tag{A1}$$

The gradients p and q were then projected onto the flow direction by computing the dot product:

$$\text{Flow-Aligned Gradient} = p \cdot \frac{v_x}{v_v} + q \cdot \frac{v_y}{v_v} \tag{A2}$$

The resulting flow-aligned gradient represents the topographic slope in the direction of flow.

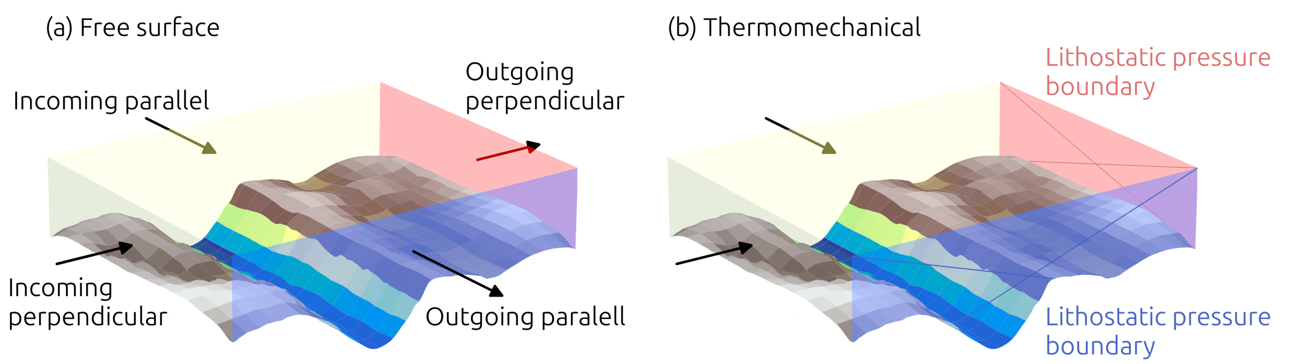

Figure A1. The incoming and outgoing boundaries for the two simulation steps **(a)** Free surface stage and **(b)** Thermomechanically coupled stage. Illustrated parallel flow direction and boundary does not represent simulated orientation.

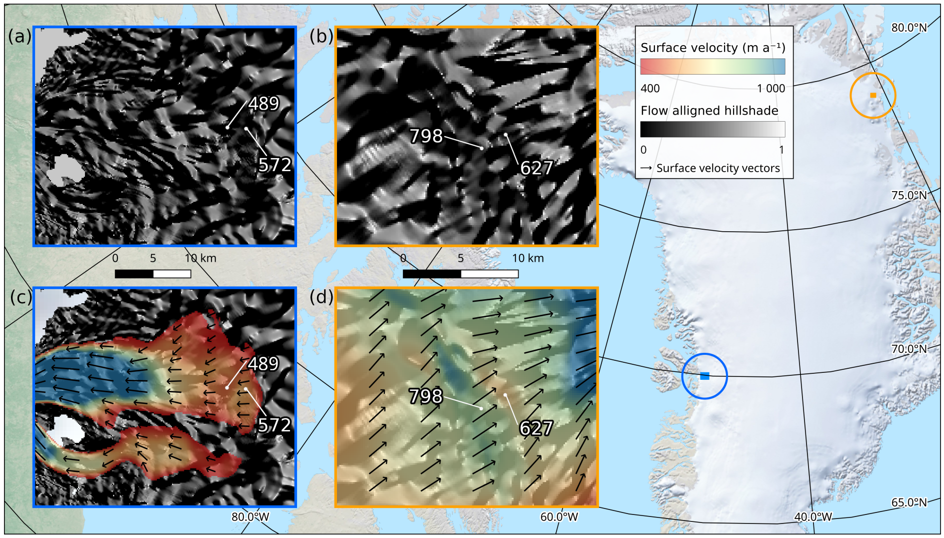

Figure A2. Two example locations in Greenland with variable surface velocity along the same flow line. **(a–b)** Hill-shade of basal topography with the azimut computed along the direction of flow (MacGregor et al., 2015). The hill-shade indicate possible areas of subglacial obstacles or valleys. **(c–d)** Surface velocity data mapped on top of the flow aligned hill-shade in **(a)** and **(b)**. Several places in the two examples have velocity differences of more than 100 m a^{-1}. Black arrows represent flow direction vectors. Velocity data from Joughin et al. (2010); Joughin (2022); Moon et al. (2023).

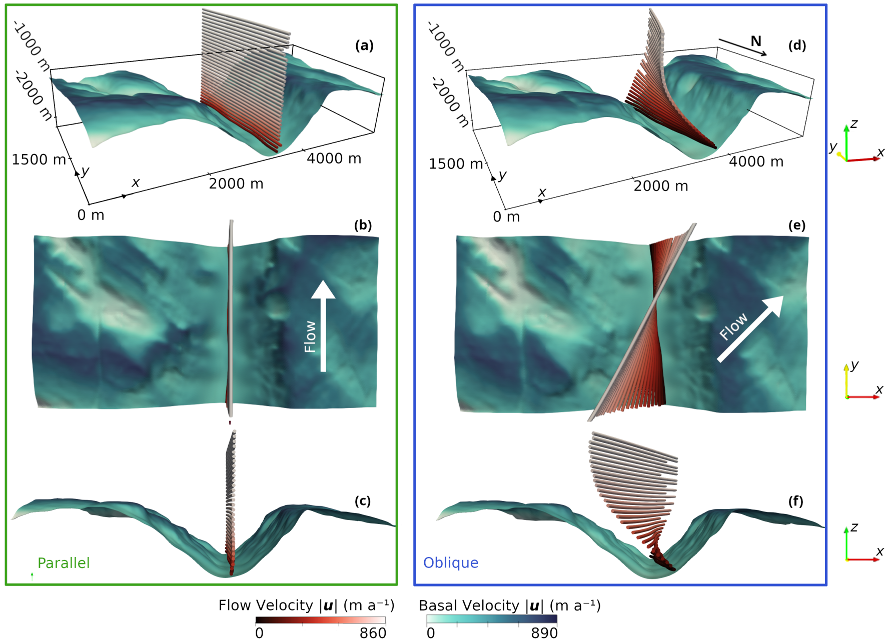

Figure A3. A comparison of parallel flow **(a)** to **(c)** from run 8Pa10, and oblique flow **(d)** to **(f)** from run 8Ob10. Both have a target velocity of 850 $\mathrm{m\,a^{-1}}$ and plateau ice thickness of 1000 m.

Table A1. Model parameters.

Symbol	Units	Variable	Value	Citation
A_1	MPa a^{-1}	Rate factor 1	9.133×10^{12}	
A_2	MPa a^{-1}	Rate factor 2	7.477×10^{23}	
A_{max}	MPa a^{-1}	Limiting rate factor		
A_s	m a^{-1} MPa^{-n}	Sliding coefficient	2.13×10^4	Average of Helanow et al. (2021) values
C		Maximum slope value	0.16167	Average of Helanow et al. (2021) values
C_a	J kg^{-1} K^{-2}	Enthalpy heat capacity A	7.253	Gilbert et al. (2014)
C_b	J kg^{-1} K^{-1}	Enthalpy heat capacity B	146.3	Gilbert et al. (2014)
G_b	W m^{-2}	Geothermal heat flux	55×10^{-3}	Cook et al. (2020)
L	J kg^{-1}	Latent heat of fusion of ice	3.34×10^5	
κ_c	kg m^{-1} a^{-1}	Cold ice enthalpy diffusivity	1.024×10^{-3}	Gilbert et al. (2014)
κ_t	kg m^{-1} a^{-1}	Temperate ice enthalpy diffusivity	1.045×10^{-4}	Gilbert et al. (2014)
p_{tr}	MPa	Triple-point pressure of water	0.612	
Q_1	J mol^{-1}	Activation energy 1	60×10^3	
Q_2	J mol^{-1}	Activation energy 2	115×10^3	
ρ_i	kg m^{-3}	Ice density	910	
T_{lim}	K	Limit temperature	263.2	Cuffey and Paterson (2010)
T_{ref}	K	Reference temperature	200	
T_{tr}	K	Triple-point temperature of water	273.2	
W_1	MPa a^{-1}	Water viscosity factor 1	1.0	Duval (1977)
W_2	MPa a^{-1}	Water viscosity factor 2	2.35	
W_3	MPa a^{-1}	Water viscosity factor 3	77.945	
ω_{lim}	Proportion	Upper water limit	0.025	

Author contributions. S Barndon ran the simulations and wrote the first version of the manuscript with support from RL and AB. TC produced scripts for Fig. 1. S Brechtelsbauer handled the conversion of geospatial data required for Fig. 1. All authors contributed to the final version of the manuscript.

Competing interests. The contact author has declared that none of the authors has any competing interests.

Acknowledgements. We thank Jan Mangerud for early discussions on flow orientations in western Norway.

References

Adams, C. J. C., Iverson, N. R., Helanow, C., Zoet, L. K., and Bate, C. E.: Softening of Temperate Ice by Interstitial Water, Frontiers in Earth Science, 9, https://doi.org/10.3389/feart.2021.702761, 2021.

Aschwanden, A., Bartholomaus, T. C., Brinkerhoff, D. J., and Truffer, M.: Brief communication: A roadmap towards credible projections of ice sheet contribution to sea level, The Cryosphere, 15, 5705–5715, https://doi.org/10.5194/tc-15-5705-2021, 2021.

Barndon, S.: Supplementary data for "Ice motion across incised fjord landscapes", https://doi.org/10.5281/zenodo.15052902, 2025.

Berends, C. J., van de Wal, R. S. W., van den Akker, T., and Lipscomb, W. H.: Compensating errors in inversions for subglacial bed roughness: same steady state, different dynamic response, The Cryosphere, 17, 1585–1600, https://doi.org/10.5194/tc-17-1585-2023, 2023.

Bernard, M., Steer, P., Gallagher, K., and Egholm, D. L.: The Impact of Lithology on Fjord Morphology, Geophysical Research Letters, 48, e2021GL093 101, https://doi.org/https://doi.org/10.1029/2021GL093101, e2021GL093101 2021GL093101, 2021.

Briner, J. P., Miller, G. H., Finkel, R., and Hess, D. P.: Glacial erosion at the fjord onset zone and implications for the organization of ice flow on Baffin Island, Arctic Canada, Geomorphology, 97, 126–134, https://doi.org/https://doi.org/10.1016/j.geomorph.2007.02.039, glacial Landscape Evolution - Implications for Glacial Processes, Patterns and Reconstructions, 2008.

Castleman, B. A., Schlegel, N.-J., Caron, L., Larour, E., and Khazendar, A.: Derivation of bedrock topography measurement requirements for the reduction of uncertainty in ice-sheet model projections of Thwaites Glacier, The Cryosphere, 16, 761–778, https://doi.org/10.5194/tc-16-761-2022, 2022.

Christ, A. J., Rittenour, T. M., Bierman, P. R., Keisling, B. A., Knutz, P. C., Thomsen, T. B., Keulen, N., Fosdick, J. C., Hemming, S. R., Tison, J.-L., Blard, P.-H., Steffensen, J. P., Caffee, M. W., Corbett, L. B., Dahl-Jensen, D., Dethier, D. P., Hidy, A. J., Perdrial, N., Peteet, D. M., Steig, E. J., and Thomas, E. K.: Deglaciation of northwestern Greenland during Marine Isotope Stage 11, Science, 381, 330–335, https://doi.org/10.1126/science.ade4248, 2023.

Cook, S. J., Christoffersen, P., Todd, J., Slater, D., and Chauché, N.: Coupled modelling of subglacial hydrology and calving-front melting at Store Glacier, West Greenland, The Cryosphere, 14, 905–924, https://doi.org/10.5194/tc-14-905-2020, 2020.

Copernicus DEM: Copernicus DEM - Global and European Digital Elevation Model, https://dataspace.copernicus.eu/explore-data/data-collections/copernicus-contributing-missions/collections-description/COP-DEM, https://doi.org/https://doi.org/10.5270/ESA-c5d3d65, [Accessed 18-03-2025], 2024.

Cuffey, K. M. and Paterson, W. S. B.: The Physics of Glaciers, Butterworth-Heinemann, Academic Press, 2010.

Duval, P.: The Role Of The Water Content On The Creep Rate Of Polycrystalline Ice., Int. Assoc. Hydrol. Sci. Publ., 118, 29–33, 1977.

Egholm, D. L., Jansen, J. D., Brædstrup, C. F., Pedersen, V. K., Andersen, J. L., Ugelvig, S. V., Larsen, N. K., and Knudsen, M. F.: Formation of plateau landscapes on glaciated continental margins, Nature Geoscience, 10, 592–597, https://doi.org/10.1038/ngeo2980, 2017.

Florinsky, I. V.: An illustrated introduction to general geomorphometry, Progress in Physical Geography, 41, 723–752, https://doi.org/10.1177/0309133317733667, 2017.

Fowler, A. C.: A theoretical treatment of the sliding of glaciers in the absense of cavitation, Philosophical Transactions of the Royal Society of London. Series A, Mathematical and Physical Sciences, 298, 637–681, https://doi.org/10.1098/rsta.1981.0003, 1981.

Frank, T., Åkesson, H., de Fleurian, B., Morlighem, M., and Nisancioglu, K. H.: Geometric controls of tidewater glacier dynamics, The Cryosphere, 16, 581–601, https://doi.org/10.5194/tc-16-581-2022, 2022.

Gagliardini, O., Cohen, D., Råback, P., and Zwinger, T.: Finite-element modeling of subglacial cavities and related friction law, Journal of Geophysical Research: Earth Surface, 112, https://doi.org/https://doi.org/10.1029/2006JF000576, 2007.

Gagliardini, O., Zwinger, T., Gillet-Chaulet, F., Durand, G., Favier, L., de Fleurian, B., Greve, R., Malinen, M., Martín, C., Råback, P., Ruokolainen, J., Sacchettini, M., Schäfer, M., Seddik, H., and Thies, J.: Capabilities and performance of Elmer/Ice, a new-generation ice sheet model, Geoscientific Model Development, 6, 1299–1318, https://doi.org/10.5194/gmd-6-1299-2013, 2013.

Gee, D. G., Fossen, H., Henriksen, N., and Higgins, A. K.: From the Early Paleozoic Platforms of Baltica and Laurentia to the Caledonide Orogen of Scandinavia and Greenland, International Union of Geological Sciences, 31, 44–51, http://episodes.org/journal/view.html?doi=10.18814/epiiugs/2008/v31i1/007, 2008.

Gilbert, A., Gagliardini, O., Vincent, C., and Wagnon, P.: A 3-D thermal regime model suitable for cold accumulation zones of polythermal mountain glaciers, Journal of Geophysical Research: Earth Surface, 119, 1876–1893, https://doi.org/https://doi.org/10.1002/2014JF003199, 2014.

Glen, J. W.: The Creep of Polycrystalline Ice, Proceedings of the Royal Society of London. Series A, Mathematical and Physical Sciences, 228, 519–538, http://www.jstor.org/stable/99642, 1955.

Gudmundsson, G. H.: Basal-flow characteristics of a non-linear flow sliding frictionless over strongly undulating bedrock, Journal of Glaciology, 43, 80–89, https://doi.org/10.3189/S0022143000002835, 1997.

Harbor, J. M.: Numerical modeling of the development of U-shaped valleys by glacial erosion, GSA Bulletin, 104, 1364–1375, https://doi.org/10.1130/0016-7606(1992)104<1364:NMOTDO>2.3.CO;2, 1992.

Harbor, J. M., Hallet, B., and Raymond, C. F.: A numerical model of landform development by glacial erosion, Nature, 333, 347–349, https://doi.org/10.1038/333347a0, 1988.

Haseloff, M., Hewitt, I. J., and Katz, R. F.: Englacial Pore Water Localizes Shear in Temperate Ice Stream Margins, Journal of Geophysical Research: Earth Surface, 124, 2521–2541, https://doi.org/https://doi.org/10.1029/2019JF005399, 2019.

Helanow, C., Iverson, N. R., Woodard, J. B., and Zoet, L. K.: A slip law for hard-bedded glaciers derived from observed bed topography, Science Advances, 7, eabe7798, https://doi.org/10.1126/sciadv.abe7798, 2021.

Hindmarsh, R. C.: Sliding over anisotropic beds, Annals of Glaciology, 30, 137–145, https://doi.org/10.3189/172756400781820840, 2000.

Iken, A.: The Effect of the Subglacial Water Pressure on the Sliding Velocity of a Glacier in an Idealized Numerical Model, Journal of Glaciology, 27, 407–421, https://doi.org/10.3189/S0022143000011448, 1981.

Joughin, I.: MEaSUREs Greenland Annual Ice Sheet Velocity Mosaics from SAR and Landsat, Version 4, https://doi.org/10.5067/RS8GFZ848ZU9, 2022.

Joughin, I., Smith, B. E., Howat, I. M., Scambos, T., and Moon, T.: Greenland flow variability from ice-sheet-wide velocity mapping, Journal of Glaciology, 56, 415–430, https://doi.org/10.3189/002214310792447734, 2010.

Jungdal-Olesen, G., Andersen, J. L., Born, A., and Pedersen, V. K.: The influence of glacial landscape evolution on Scandinavian ice-sheet dynamics and dimensions, The Cryosphere, 18, 1517–1532, https://doi.org/10.5194/tc-18-1517-2024, 2024.

Kartverket: Depth data from the Norwegian Mapping Authority (Kartverket), https://kartkatalog.geonorge.no/metadata/kartverket/dybdedata-terrengmodeller-dtm-wcs/8896c751-f3e0-4e4c-86e2-7579cea1f111, 2024a.

Kartverket: Elevation data from the Norwegian Mapping Authority (Kartverket), https://hoydedata.no/LaserInnsyn2/, 2024b.

Kessler, M. A., Anderson, R. S., and Briner, J. P.: Fjord insertion into continental margins driven by topographic steering of ice, Nature Geoscience, 1, 365–369, https://doi.org/10.1038/ngeo201, 2008.

Kleman, J., Hättestrand, C., Borgström, I., and Stroeven, A.: Fennoscandian palaeoglaciology reconstructed using a glacial geological inversion model, Journal of Glaciology, 43, 283–299, https://doi.org/10.3189/S0022143000003233, 1997.

Kyrke-Smith, T. M., Gudmundsson, G. H., and Farrell, P. E.: Relevance of Detail in Basal Topography for Basal Slipperiness Inversions: A Case Study on Pine Island Glacier, Antarctica, Frontiers in Earth Science, 6, https://doi.org/10.3389/feart.2018.00033, 2018.

Law, R., Christoffersen, P., MacKie, E., Cook, S., Haseloff, M., and Gagliardini, O.: Complex motion of Greenland Ice Sheet outlet glaciers with basal temperate ice, Science Advances, 9, eabq5180, https://doi.org/10.1126/sciadv.abq5180, 2023.

Lliboutry, L.: General Theory of Subglacial Cavitation and Sliding of Temperate Glaciers, Journal of Glaciology, 7, 21–58, https://doi.org/10.3189/S0022143000020396, 1968.

Lliboutry, L.: Realistic, yet simple bottom boundary conditions for glaciers and ice sheets, Journal of Geophysical Research: Solid Earth, 92, 9101–9109, https://doi.org/https://doi.org/10.1029/JB092iB09p09101, 1987.

Løkkegaard, A., Mankoff, K. D., Zdanowicz, C., Clow, G. D., Lüthi, M. P., Doyle, S. H., Thomsen, H. H., Fisher, D., Harper, J., Aschwanden, A., Vinther, B. M., Dahl-Jensen, D., Zekollari, H., Meierbachtol, T., McDowell, I., Humphrey, N., Solgaard, A., Karlsson, N. B., Khan, S. A., Hills, B., Law, R., Hubbard, B., Christoffersen, P., Jacquemart, M., Seguinot, J., Fausto, R. S., and Colgan, W. T.: Greenland and Canadian Arctic ice temperature profiles database, The Cryosphere, 17, 3829–3845, https://doi.org/10.5194/tc-17-3829-2023, 2023.

MacGregor, J. A., Fahnestock, M. A., Catania, G. A., Paden, J. D., Prasad Gogineni, S., Young, S. K., Rybarski, S. C., Mabrey, A. N., Wagman, B. M., and Morlighem, M.: Radiostratigraphy and age structure of the Greenland Ice Sheet, Journal of Geophysical Research: Earth Surface, 120, 212–241, https://doi.org/https://doi.org/10.1002/2014JF003215, 2015.

MacGregor, J. A., Colgan, W. T., Paxman, G. J. G., Tinto, K. J., Csathó, B., Darbyshire, F. A., Fahnestock, M. A., Kokfelt, T. F., MacKie, E. J., Morlighem, M., and Sergienko, O. V.: Geologic Provinces Beneath the Greenland Ice Sheet Constrained by Geophysical Data Synthesis, Geophysical Research Letters, 51, e2023GL107 357, https://doi.org/https://doi.org/10.1029/2023GL107357, e2023GL107357 2023GL107357, 2024.

Maier, N., Gimbert, F., Gillet-Chaulet, F., and Gilbert, A.: Basal traction mainly dictated by hard-bed physics over grounded regions of Greenland, The Cryosphere, 15, 1435–1451, https://doi.org/10.5194/tc-15-1435-2021, 2021.

Mangerud, J., Hughes, A. L., Sæle, T. H., and Svendsen, J. I.: Ice-flow patterns and precise timing of ice sheet retreat across a dissected fjord landscape in western Norway, Quaternary Science Reviews, 214, 139–163, https://doi.org/https://doi.org/10.1016/j.quascirev.2019.04.032, 2019.

Meyer, C. R. and Creyts, T. T.: Formation of ice eddies in subglacial mountain valleys, Journal of Geophysical Research: Earth Surface, 122, 1574–1588, https://doi.org/https://doi.org/10.1002/2017JF004329, 2017.

Minchew, B. and Joughin, I.: Toward a universal glacier slip law, Science, 368, 29–30, https://doi.org/10.1126/science.abb3566, 2020.

Moffatt, H.: Viscous eddies near a sharp corner(Viscous eddy behavior near sharp corner, considering outer boundary conditions and stream function), Archiwum Mechaniki Stosowanej, 16, 365–372, 1964a.

Moffatt, H. K.: Viscous and resistive eddies near a sharp corner, Journal of Fluid Mechanics, 18, 1–18, https://doi.org/10.1017/S0022112064000015, 1964b.

Moon, T. A., Fisher, M., Stafford, T., and Thurber, A.: QGreenland (v3) [dataset], National Snow and Ice Data Center., https://qgreenland.org, 2023.

Morlighem, M., Williams, C. N., Rignot, E., An, L., Arndt, J. E., Bamber, J. L., Catania, G., Chauché, N., Dowdeswell, J. A., Dorschel, B., Fenty, I., Hogan, K., Howat, I., Hubbard, A., Jakobsson, M., Jordan, T. M., Kjeldsen, K. K., Millan, R., Mayer, L., Mouginot, J., Noël, B. P. Y., O'Cofaigh, C., Palmer, S., Rysgaard, S., Seroussi, H., Siegert, M. J., Slabon, P., Straneo, F., van den Broeke, M. R., Weinrebe, W., Wood, M., and Zinglersen, K. B.: BedMachine v3: Complete Bed Topography and Ocean Bathymetry Mapping of

Greenland From Multibeam Echo Sounding Combined With Mass Conservation, Geophysical Research Letters, 44, 11,051–11,061, https://doi.org/https://doi.org/10.1002/2017GL074954, 2017.

Nye, J. F.: The Flow Law of Ice from Measurements in Glacier Tunnels, Laboratory Experiments and the Jungfraufirn Borehole Experiment, Proceedings of the Royal Society of London. Series A, Mathematical and Physical Sciences, 219, 477–489, http://www.jstor.org/stable/99248, 1953.

Ottesen, D., Dowdeswell, J. A., and Rise, L.: Submarine landforms and the reconstruction of fast-flowing ice streams within a large Quaternary ice sheet: The 2500-km-long Norwegian-Svalbard margin (57° - 80°N), Geological Society of America Bulletin, 117, 1033–1050, https://doi.org/https://doi.org/10.1130/B25577.1, 2005.

Paxman, G. J.: Patterns of valley incision beneath the Greenland Ice Sheet revealed using automated mapping and classification, Geomorphology, 436, 108 778, https://doi.org/https://doi.org/10.1016/j.geomorph.2023.108778, 2023.

Paxman, G. J. G., Jamieson, S. S. R., Dolan, A. M., and Bentley, M. J.: Subglacial valleys preserved in the highlands of south and east Greenland record restricted ice extent during past warmer climates, The Cryosphere, 18, 1467–1493, https://doi.org/10.5194/tc-18-1467-2024, 2024.

Reilly, E.: Ice Flow as an Indicator of Ice Thickness, Master of science thesis in quarternary geology, University of Bergen, 2023.

Roldán-Blasco, J.-P., Gilbert, A., Piard, L., Gimbert, F., Vincent, C., Gagliardini, O., Togaibekov, A., Walpersdorf, A., and Maier, N.: Creep enhancement and sliding in a temperate, hard-bedded alpine glacier, The Cryosphere, 19, 267–282, https://doi.org/10.5194/tc-19-267-2025, 2025.

Schohn, C. M., Iverson, N. R., Zoet, L. K., Fowler, J. R., and Morgan-Witts, N.: Linear-viscous flow of temperate ice, Science, 387, 182–185, https://doi.org/10.1126/science.adp7708, 2025.

Schoof, C.: The effect of cavitation on glacier sliding, Proceedings of the Royal Society A: Mathematical, Physical and Engineering Sciences, 461, 609–627, https://doi.org/10.1098/rspa.2004.1350, 2005.

Schoof, C. and Hewitt, I. J.: A Model for Polythermal Ice Incorporating Gravity-Driven Moisture Transport, Journal of Fluid Mechanics, 797, 504–535, https://doi.org/10.1017/jfm.2016.251, 2016.

Sergienko, O. V., Creyts, T. T., and Hindmarsh, R. C. A.: Similarity of organized patterns in driving and basal stresses of Antarctic and Greenland ice sheets beneath extensive areas of basal sliding, Geophysical Research Letters, 41, 3925–3932, https://doi.org/https://doi.org/10.1002/2014GL059976, 2014.

Svendsen, J. I. and Mangerud, J.: Late Weichselian and holocene sea-level history for a cross-section of western Norway, Journal of Quaternary Science, 2, 113–132, https://doi.org/https://doi.org/10.1002/jqs.3390020205, 1987.

Tsai, V. C., Stewart, A. L., and Thompson, A. F.: Marine ice-sheet profiles and stability under Coulomb basal conditions, Journal of Glaciology, 61, 205–215, https://doi.org/10.3189/2015JoG14J221, 2015.

Weertman, J.: On the Sliding of Glaciers, Journal of Glaciology, 3, 33–38, https://doi.org/10.3189/S0022143000024709, 1957.

Weertman, J.: The Unsolved General Glacier Sliding Problem, Journal of Glaciology, 23, 97–115, https://doi.org/10.3189/S0022143000029762, 1979.

Wernecke, A., Edwards, T. L., Holden, P. B., Edwards, N. R., and Cornford, S. L.: Quantifying the Impact of Bedrock Topography Uncertainty in Pine Island Glacier Projections for This Century, Geophysical Research Letters, 49, e2021GL096 589, https://doi.org/https://doi.org/10.1029/2021GL096589, e2021GL096589 2021GL096589, 2022.

Young, D. A., Wright, A. P., Roberts, J. L., Warner, R. C., Young, N. W., Greenbaum, J. S., Schroeder, D. M., Holt, J. W., Sugden, D. E., Blankenship, D. D., van Ommen, T. D., and Siegert, M. J.: A dynamic early East Antarctic Ice Sheet suggested by ice-covered fjord landscapes, Nature, 474, 72–75, https://doi.org/10.1038/nature10114, 2011.

Zoet, L. K. and Iverson, N. R.: A slip law for glaciers on deformable beds, Science, 368, 76–78, https://doi.org/10.1126/science.aaz1183, 2020.